PROCEEDINGS A

royalsocietypublishing.org/journal/rspa

Research

Cite this article: Cuomo F, Ferruzzi J, Agarwal P, Li C, Zhuang ZW, Humphrey JD, Figueroa CA. 2019 Sex-dependent differences in central artery haemodynamics in normal and fibulin-5 deficient mice: implications for ageing. *Proc. R. Soc. A* **475**: 20180076. http://dx.doi.org/10.1098/rspa.2018.0076

Received: 5 February 2018
Accepted: 26 November 2018

Subject Areas:
biomedical engineering, biomechanics

Keywords:
aorta, stiffness, mechanics, fluid–solid interaction, pulse pressure, pulse wave velocity

Author for correspondence:
C. Alberto Figueroa
e-mail: figueroc@med.umich.edu

†These authors contributed equally to this study.

Electronic supplementary material is available online at https://dx.doi.org/10.6084/m9.figshare.c.4342259.

THE ROYAL SOCIETY PUBLISHING

Sex-dependent differences in central artery haemodynamics in normal and fibulin-5 deficient mice: implications for ageing

Federica Cuomo[1,†], Jacopo Ferruzzi[3,†], Pradyumn Agarwal[1], Chen Li[1], Zhen W. Zhuang[4], Jay D. Humphrey[3,5] and C. Alberto Figueroa[1,2]

[1]Department of Biomedical Engineering, and [2]Department of Surgery, University of Michigan, Ann Arbor, MI, USA
[3]Department of Biomedical Engineering, [4]Translational Research Imaging Center, and [5]Vascular Biology and Therapeutics Program, Yale University, New Haven, CT, USA

JDH, 0000-0003-1011-2025; CAF, 0000-0002-3934-6506

Mouse models provide unique opportunities to study vascular disease, but they demand increased experimental and computational resolution. We describe a workflow for combining *in vivo* and *in vitro* biomechanical data to build mouse-specific computational models of the central vasculature including regional variations in biaxial wall stiffness, thickness and perivascular support. These fluid–solid interaction models are informed by micro-computed tomography imaging and *in vivo* ultrasound and pressure measurements, and include mouse-specific inflow and outflow boundary conditions. Hence, the model can capture three-dimensional unsteady flows and pulse wave characteristics. The utility of this experimental–computational approach is illustrated by comparing central artery biomechanics in adult wild-type and fibulin-5 deficient mice, a model of early vascular ageing. Findings are also examined as a function of sex. Computational results compare well with measurements and data available in the literature and suggest that pulse wave velocity, a spatially integrated measure of arterial stiffness, does not reflect well the presence of regional differences in stiffening, particularly those manifested in male versus female mice. Modelling results are also useful for comparing quantities that are difficult to

measure or infer experimentally, including local pulse pressures at the renal arteries and characteristics of the peripheral vascular bed that may differ with disease.

1. Introduction

Ageing is a primary risk factor for increased central artery stiffness [1], which in turn is a strong indicator and initiator of cardiovascular, neurovascular and renovascular disease [2]. Arterial ageing in humans associates with many changes in cellular activity and extracellular matrix architecture, including a progressive loss of elastic fibre integrity [3]. That is, the ageing phenotype results in part from mechanical damage to and proteolytic degradation of elastic fibres, which we have shown can decrease collagen fibre undulation and thereby exacerbate the arterial stiffening [4]. Notwithstanding the availability of considerable histopathological, biomechanical and clinical data on the effects of ageing of the central vasculature in humans, it is difficult to obtain detailed information on evolving regional mechanical properties [5,6] and associated effects on the haemodynamics [7]. For this reason, mouse models have become increasingly important in studying vascular health and disease.

Old mice exhibit a vascular ageing phenotype [8,9], but not as a result of significant changes in elastic fibre integrity because of the combination of a short lifespan and the long normal half-life of vascular elastin [10]. We have shown, however, that genetically modified mouse models can be used to study the effects of graded losses in elastic fibre integrity, with the fibulin-5 deficient mouse displaying the most dramatic elastopathy in the common carotid artery of multiple viable models of elastic fibre-associated mutations that we studied [11]. Indeed, it appears that this mouse represents a model of early, stable vascular ageing [12]. Fibulin-5 is a glycoprotein that associates with elastin to form elastic fibres, and it is thought to function largely in elastogenesis. Histological evidence reveals disrupted elastic laminae in these mice, primarily in the outer portion of the media.

The current clinical gold standard measure of central artery stiffness is the pulse wave velocity (*PWV*), often measured from the carotid to the femoral artery [2]. The Moens–Korteweg relation reveals that *PWV* depends on the intrinsic material stiffness of the wall as well as wall thickness and luminal radius. This relation assumes that each of these quantities is spatially uniform, however, which is clearly not the case over substantial lengths of the central vasculature. There is a pressing need, therefore, to assess better the potential effects of regional variations in central arterial geometry and mechanical properties on the haemodynamics that can adversely affect the microcirculation in the heart, brain and kidneys. Towards this end, one can combine *in vitro* (mechanical properties) and *in vivo* (geometric and haemodynamic) data with sophisticated computational models to account directly for regional variations along the central vasculature. Such computations can provide information not otherwise measured easily and can help build intuition that is helpful in interpreting clinically available results.

In this paper, we meld *in vitro* information from regional biaxial mechanical testing of five different central arteries with *in vivo* information from non-invasive micro-computed tomography (CT) and ultrasound as well as invasive catheterization to build computational haemodynamic models of the central vasculature in four different animal groups: male and female wild-type and fibulin-5 deficient mice. Specifically, we perform fluid–solid interaction (FSI) simulations over the central vasculature and compare associated regional flows and pressure waves as well as computed pulse wave velocities. Notwithstanding significant advantages of studies in mice, there are also challenges. Small perturbations in anaesthesia and temperature can introduce variability in measurements within and across animals. Furthermore, because many of the requisite experimental procedures are terminal, it is difficult to obtain data on biaxial stiffness, aortic anatomy and haemodynamics from the same mouse, making it challenging to perform truly mouse-specific FSI haemodynamic simulations informed by the aforementioned data. In this paper, we propose a strategy to assign haemodynamic and structural stiffness data

for four different groups of mice to individual micro-CT aortic models to produce calibrated computational results that provide general insights into quantities not easily obtained through experiments, such as pressure indices in the renal arteries or values of peripheral resistance and compliance, which can then be compared across diverse groups.

2. Methods

All animal procedures were approved by the Institutional Animal Care and Use Committee (IACUC) of Yale University, New Haven, CT, USA. Homozygous *Fbln5*$^{+/+}$ (WT) and *Fbln5*$^{-/-}$ knockout (KO) mice were generated by breeding heterozygous *Fbln5*$^{+/-}$ pairs on a mixed C57BL/6 × 129/SvEv background. The animals were divided into four groups to investigate the effects of sex and genotype: WT males (WT_M), WT females (WT_F), KO males (KO_M) and KO females (KO_F). All animals were 20–22 weeks of age, except for one 36-week-old male KO mouse. Owing to the impracticality of collecting complete *in vivo* and *in vitro* datasets from any single animal, these four basic experimental groups were divided into three cohorts (figure 1):

— An anatomy cohort, for which we collected non-invasive *in vivo* micro-CT data on the temporal mean vascular geometry.
— A wall mechanics cohort, for which we collected regional *in vitro* biaxial data on five central vessels: the common carotid artery (CCA) as well as the ascending thoracic aorta (ATA), descending thoracic aorta (DTA), suprarenal abdominal aorta (SAA) and infrarenal abdominal aorta (IAA).
— A haemodynamics cohort, for which we collected non-invasive *in vivo* ultrasound data on cyclic changes in geometry and flow as well as invasive *in vivo* data on cyclic pressures.

External factors that can influence such measurements, such as age and body mass, and similarly the type and level of anaesthesia, heart rate and body temperature were kept as consistent as possible across all four groups. Our overall strategy to build mouse-specific computational models was as follows: regional wall mechanics data were assigned to each micro-CT anatomical model using values of local radii and previously obtained material properties and wall thicknesses for each of the four groups [13] while haemodynamics data were mapped to each model using body mass based allometric scaling of quantities such as cardiac output (CO), total arterial resistance and total arterial compliance. Therefore, this workflow relied on 'group-specific' data to prescribe the parameters needed to perform FSI analyses for each specific member of the anatomy cohort. For the sake of simplicity, we refer to the output of this workflow as 'mouse-specific' given the individual micro-CT scans, even though it relies on mass and radius scaling laws for each of the four animal groups considered.

(a) Experimental procedure

(i) Anatomy

Briefly, mice were anaesthetized using 1–2% isoflurane, then given a bolus intravenous (jugular vein) injection of a nanoemulsion formulation (Fenestra VC, MediLumine Inc., Montreal, CA), at a dose of 0.2 ml/20 g, as a blood-pool contrast agent designed for prolonged vascular imaging. Immediately thereafter, the animal was placed prone inside a micro-CT scanner (eXplore CT120; GE Healthcare) for non-gated whole body scanning. The images were reconstructed as isotropic $49 \times 49 \times 49\ \mu m^3$ voxels. All reconstructions were done with a Feldkamp algorithm and all images were calibrated with standard Hounsfield units (HU) using microView. A relatively constant heart rate (±10%) was achieved by careful maintenance of the level of isoflurane anaesthesia and body temperature during each scan. Image data were collected for $n = 3$ mice per group, except for the KO_F group for which $n = 2$. Hence, $n = 11$ mice were imaged. These specimens were used to define the anatomical models (figure 2).

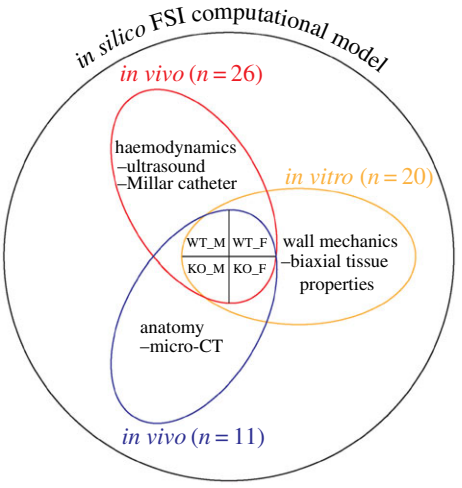

Figure 1. Three experimental cohorts of mice were used to acquire data on haemodynamics, wall properties and aortic anatomy for four groups of mice: adult male and female homozygous *Fbln5*$^{+/+}$ (WT) and *Fbln5*$^{-/-}$ (KO) mice. The experimental data were synthesized to create an *in silico* FSI computational model of the unsteady haemodynamics and regional wall mechanics. (Online version in colour.)

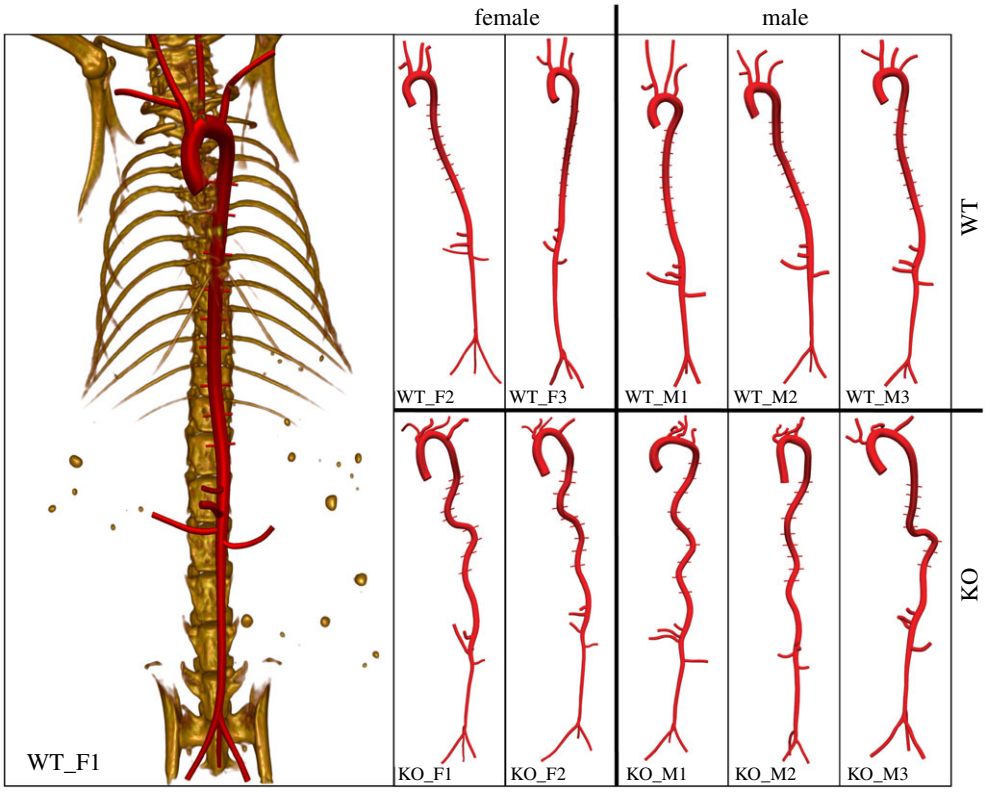

Figure 2. Anatomical models created for each of the four groups: female and male WT and KO. The KO mice had a marked increase in aortic tortuosity, particularly in the DTA. All animals were 20–22 weeks of age, except for one 36-week-old male KO mouse (KO_M3). The image for WT_F1 shows the associated skeleton, which although not shown for the other 10 cases was nevertheless used to locate the pairs of intercostal branches that were not visible on the micro-CT scans. (Online version in colour.)

(ii) Wall mechanics

As reported previously [13], biaxial material properties were estimated at four different locations along the aorta (ATA, DTA, SAA and IAA) and within one CCA using data collected via a custom computer-controlled biaxial testing device [14]. Briefly, following standard preconditioning, seven cyclic loading protocols were performed: cyclic pressure diameter tests from 10 to 140 mmHg at three different fixed values of axial stretch (95%, 100%, 105% of the *in vivo* value) and cyclic axial extension tests at four fixed values of transmural pressure (10, 60, 100 and 140 mmHg). Best-fit values of the eight model parameters within a 'four-fibre family' constitutive model were determined for $n = 5$ animals per group (for a total of $n = 20$ mice) using a nonlinear regression algorithm to minimize the difference between predicted and measured pressure–diameter and axial force–stretch data from the last unloading cycle of all seven testing protocols.

(iii) Haemodynamics

Following inhalation anaesthesia, the mouse was gently laid on its back and secured on a surgical platform with a recirculating heating pad (TP-500 Heat Therapy Pump; Gaymar Industries Inc., Orchard Park, NY) to maintain body temperature. Next, the midline thorax and abdomen were shaved and an ultrasound gel applied. Mean blood velocity and luminal diameters were then acquired via ultrasound (Vevo 2100 system; Fujifilm VisualSonics) within the ATA, IAA and CCA. CO was measured similarly with transthoracic echocardiography, then central aortic pressure was measured using an SPR-1000 Millar pressure catheter. A total of $n = 26$ mice were studied across the four groups.

(b) Computational

We employed the custom computational haemodynamics framework CRIMSON [15] to perform the FSI studies. These simulations included three-dimensional anatomical models of the aorta and main branches, spatially variable mechanical properties of the central vasculature, three-element Windkessel models used as outflow boundary conditions for each branch of the anatomical models, and an external tissue support formulation to simulate the effects of perivascular tissue on aortic haemodynamics. We also used *a posteriori* gradient-based mesh adaptation methods for iterative mesh refinement [16]. Blood viscosity was $0.004\,\mathrm{kg\,m^{-1}\,s^{-1}}$ and blood density was $1060\,\mathrm{kg\,m^{-3}}$. Below we describe the workflow used to meld into single computational models the experimental data acquired in the three cohorts of mice (figure 1).

(i) Anatomical models

Three-dimensional anatomical models of the central vasculature were reconstructed from the micro-CT image data using the CRIMSON GUI. A two-dimensional semi-automatic segmentation procedure followed by three-dimensional lofting generated a non-uniform rational basis splines (NURBS) description of each vasculature. Briefly, centreline paths were identified from the micro-CT images and two-dimensional contours were drawn, with discrete spacing, perpendicular to each path to define the vessel lumen at the two-dimensional contour locations. Contours were then lofted to create three-dimensional volumes for each vessel (i.e. aorta and primary branches) and a union operation was used to merge individual vessels into a single analytical geometric model. The aortic root was not always discernible in the images, thus the length of the ATA was adjusted for each model according to the mean *in vivo* axial length measured with ultrasound for that group. Lastly, nine pairs of intercostal arteries (not visible in the image data) were added to each model using the location of the ribs as a reference, resulting in $n = 11$ anatomical models (figure 2).

Field-driven mesh adaptation techniques were employed to refine the finite-element meshes in areas of expected large velocity gradients [16]. The final unstructured field-adapted meshes ranged between 1.4×10^6 tetrahedral elements, with 2.5×10^4 nodes, to 2.2×10^6 tetrahedral elements, with 4.0×10^5 nodes.

(ii) Wall mechanics and biaxial tissue properties

One needs an FSI method to capture pulse wave propagation within a distensible vasculature. Toward this end, we employed a coupled momentum formulation [17] and modelled each vascular segment as an incompressible elastic membrane of thickness h characterized by a 5×5 stiffness matrix that was linearized about the mean arterial pressure [18], with all quantities varying from region to region. Specifically, the regionally dependent values of material stiffness were determined from a nonlinear, anisotropic stored energy function using the theory of small deformations superimposed on large [19], which naturally accounts for regionally dependent values of the *in vivo* axial extension and circumferential distension at mean arterial pressure. The axial stretch was estimated via the cross-over point in the *in vitro* force–length tests performed at four different pressures [20], whereas the circumferential stretch was calculated from the *in vivo* diameter assessed by micro-CT and the unloaded diameter measured *ex vivo*. It should be noted, however, that the ATA also experiences a cyclic axial extension throughout the cardiac cycle of the same order of magnitude as the cyclic circumferential distension. The mean axial stretch of the ATA was estimated from micro-CT measured lengths *in vivo* and unloaded lengths measured *in vitro*.

The regionally dependent mean values of wall stiffness and thickness are listed in the electronic supplementary material, table S1. They were mapped directly onto segments of each anatomical model at the following five regions: ATA, DTA, SAA, IAA and CCA. Values within the DTA were further subdivided into proximal and distal segments (pDTA and dDTA) using individual stretches. Values elsewhere were populated by linearly interpolating values at the aforementioned six sites.

Most arteries are supported externally by perivascular tissues, which constrain vascular motions via an effective external pressure (P_{EXT}). A traction boundary condition was applied on the outer vascular wall to mimic the effects of a distributed viscoelastic stress imparted by perivascular tissue or organs. Specifying this viscoelastic stress requires two spatially distributed parameters: a stiffness coefficient (k_{s}) and a damping coefficient (c_{s}). The parameter k_{s} was estimated using an iterative approach for each aortic location (described in the electronic supplementary material, table S2) while the value of c_{s} was simply set to the minimum value that eliminated spurious oscillations in the computed wall motion. Final values for k_{s} and P_{EXT} are listed in the electronic supplementary material, table S2.

(iii) Haemodynamics

Mouse-specific haemodynamic data were assigned to micro-CT based anatomical models separately for each of the four groups using allometric scaling of quantities such as CO, total arterial resistance and total arterial compliance. Allometric scaling laws are of the form: $Y = Y_0 M^b$, where Y is the quantity of interest, Y_0 is a normalization constant, M is the body mass and b is a scaling exponent. Allometric scaling can be used within a species or across species, with coefficients determined by plotting the quantities of interest against body mass in log–log plots and performing linear regressions of the form $\log(Y) = \log(Y_0) + b * \log(M)$ [21]. This scaling was used to inform the inlet and peripheral boundary conditions for each specimen.

Inlet boundary conditions. Velocity and diameter data measured with ultrasound at the ATA were used to calculate a time-averaged flow waveform for each mouse ($n = 26$) within the haemodynamics cohort. Each flow waveform was then Fourier interpolated using 36 modes. Waveforms showing artefacts such as spurious systolic oscillations or lack of diastolic backflow were disregarded. The remaining waveforms were aligned at the peak diastolic backflow and averaged. This procedure produced a single flow waveform template using data across the four groups (WT_M, WT_F, KO_M and KO_F) that was then scaled for each micro-CT anatomy as follows. Allometric scaling of CO was performed separately for the four groups (figure 3*a*) with CO measured using two different techniques: echocardiographic changes in left ventricular volume (blue dots in the figure) and ultrasonic-derived velocity and diameter measurements in the ATA (red dots), each over multiple cardiac cycles. Three measurements

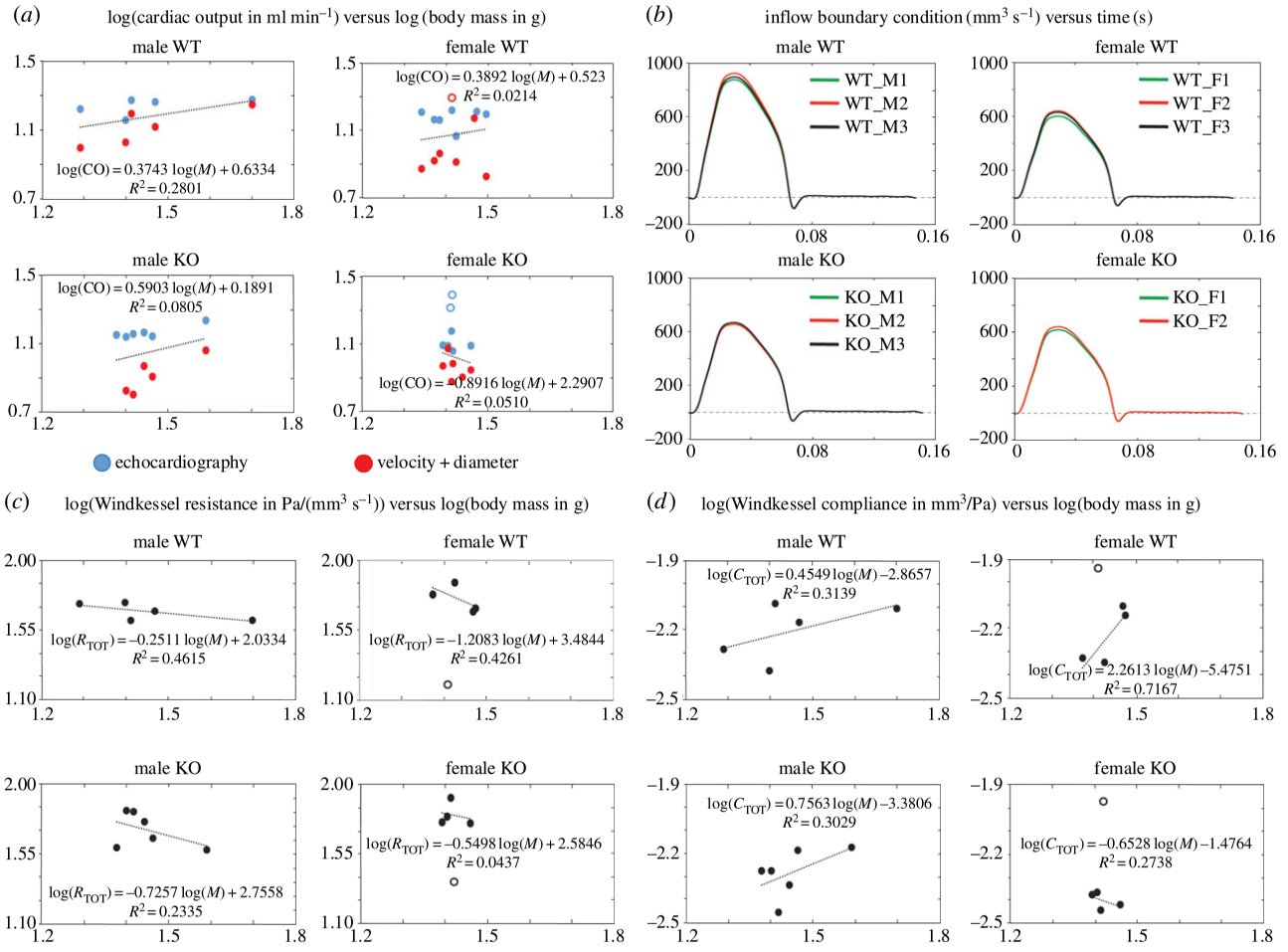

Figure 3. (*a*) Allometric scaling of CO for each of the four groups based on echocardiographic and ultrasound-derived velocity and diameter data. (*b*) Mouse-specific flow waveforms mapped to each specimen in the anatomy cohort. (*c*) Allometric scaling of total arterial resistance (R_{TOT}) for each of the four groups. (*d*) Allometric scaling of total arterial compliance (C_{TOT}) for each of the four groups.

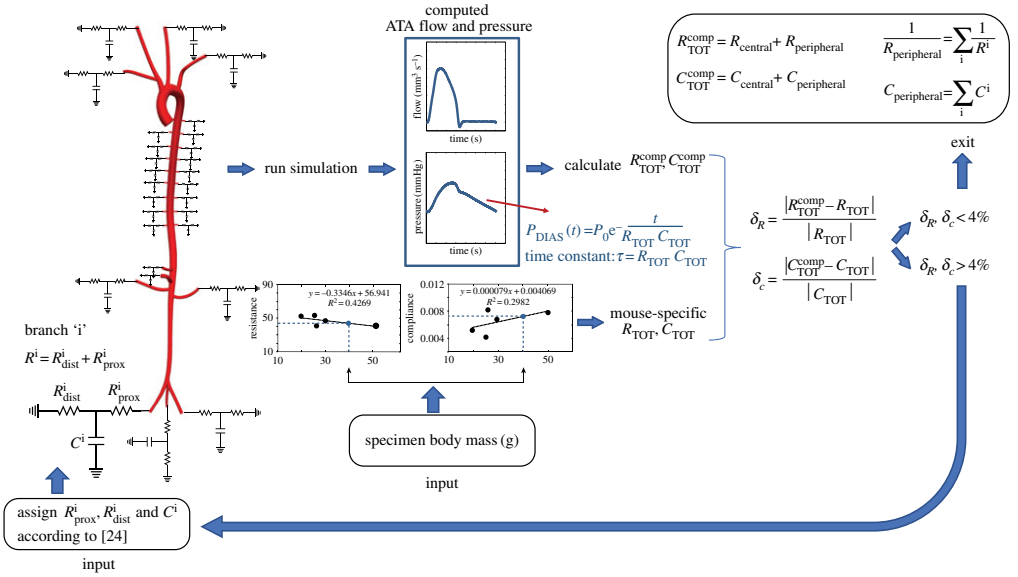

Figure 4. Workflow for mouse-specific peripheral boundary conditions. For each of the 26 mice in the haemodynamics cohort, R_{TOT} and C_{TOT} were estimated from the measured ATA pressure and flow waveforms by $R_{TOT} = P_{MEAN}/CO$ with C_{TOT} then determined by fitting the diastolic portion of the pressure waveform with an exponential decay function ($P_{DIAS}(t) = \exp(-t/R_{TOT}C_{TOT})$) [22,23]. Using allometric scaling, specific values of R_{TOT} and C_{TOT} were then prescribed for each of the 11 mice in the anatomy cohort. Values of R^i_{prox}, R^i_{dist} and C^i were estimated iteratively following a prior method [24] for each vessel 'i' until the computed total central resistance and compliance $R^{comp}{}_{TOT}$ and $C^{comp}{}_{TOT}$ matched the experimental values R_{TOT} and C_{TOT}. (Online version in colour.)

were considered outliers and excluded from the regression (empty circles in figure 3*a*): two echocardiographic measurements in KO females and one velocity + diameter measurement in a WT female. Allometric scaling for each group makes it possible to assign mouse-specific values of CO to each of the specimens in the four different groups.

Additional considerations for CO scaling. Haemodynamic data for flow and pressure were acquired under different experimental conditions, representing different degrees of invasiveness. Mean blood velocity and diameter were measured non-invasively with ultrasound while central aortic pressure was measured invasively with a catheter, both under similar levels of anaesthesia. In a previous study, we investigated the haemodynamic impact of catheters placed within the murine aorta and observed a reduction in CO [18] relative to conditions without a catheter. Therefore, we further scaled down the estimated CO for each animal by 7% across the four groups. The mouse-specific values of CO were then mapped to the common flow waveform template, resulting in flow waveforms for each of the four groups (figure 3*b*).

Peripheral boundary conditions. We used a multiscale approach to prescribe outflow boundary conditions. Lumped parameter models of the distal circulation were coupled to each outlet surface for each mouse-specific model: total arterial resistance (R_{TOT}) and total arterial compliance (C_{TOT}) were estimated from measured ATA pressure and flow waveforms for each mouse in the haemodynamics cohort [22]. Namely, $R_{TOT} = P_{MEAN}/CO$, whereas C_{TOT} was determined by fitting the diastolic part of the pressure waveform with an exponential decay $P_{DIAS}(t) = \exp(-t/R_{TOT}C_{TOT})$ [23]. Allometric scaling of R_{TOT} and C_{TOT} was then performed for each mouse in the anatomic cohort (figure 3*c*,*d*). Figure 4 illustrates the overall workflow for specifying mouse-specific outflow boundary conditions. Two key inputs are:

1. Specific values of R_{TOT} and C_{TOT} (table 1) were prescribed for each of the 11 mice in the anatomy cohort based on their body mass. R_{TOT} and C_{TOT} were then decomposed into

Table 1. Body mass and corresponding adjusted values of CO, total resistance (R_{TOT}) and total compliance (C_{TOT}) assigned to each computational model via allometric scaling. Body mass (g); CO (ml min^{-1}); R_{TOT} (Pa/(mm^3 s^{-1})); C_{TOT} (mm^3 Pa^{-1}).

wild-type_male (WT_M)					wild-type_female (WT_F)				
mouse	body mass	CO	R_{TOT}	C_{TOT}	mouse	body mass	CO	R_{TOT}	C_{TOT}
WT_M1	33	14.8	44.8	0.0067	WT_F1	23	10.5	69.0	0.0040
WT_M2	38	15.6	43.2	0.0071	WT_F2	27	11.2	56.9	0.0058
WT_M3	35	15.2	44.1	0.0069	WT_F3	26	11.0	59.5	0.0053
mean	36	15.2	44.1	0.0069	mean	25[a]	10.9[a]	61.8[a]	0.0050[a]
s.d.	3	0.4	0.8	0.0002	s.d.	2	0.4	6.4	0.0009
knockout_male (KO_M)					knockout_female (KO_F)				
mouse	body mass	CO	R_{TOT}	C_{TOT}	mouse	body mass	CO	R_{TOT}	C_{TOT}
KO_M1	31	10.9	47.2	0.0056	KO_F1	25	10.3	65.5	0.0041
KO_M2	30	10.9	48.3	0.0055	KO_F2	24	10.7	67.0	0.0042
KO_M3	31	10.7	47.2	0.0056	—	—	—	—	—
mean	31[b]	10.9[b]	47.5	0.0056[b]	mean	24[a]	10.5	66.2[a]	0.0041[a]
s.d.	1	0.1	0.7	0.0001	s.d.	1	0.3	1.1	0.0001

[a] $p < 0.05$ between M and F of the same genotype.
[b] $p < 0.05$ between WT and KO of the same sex.

the sum of components representing central ($R_{central}$, $C_{central}$) and peripheral ($R_{peripheral}$, $C_{peripheral}$) contributions:

$$R_{TOT} = R_{central} + R_{peripheral}$$

and

$$C_{TOT} = C_{central} + C_{peripheral},$$

where $R_{central}$ and $C_{central}$ are set by the anatomy and tissue properties of the specimen.

2. Three-element Windkessel (RCR) models were coupled to each outlet branch 'i', each characterized by a resistance R^i (divided between proximal R^i_{prox} and distal R^i_{dist} resistances) and a compliance C^i. Initial estimates for these parameters were obtained as detailed in [24]. The following method was used to evaluate $R_{peripheral}$ and $C_{peripheral}$ for each of the 11 mice. A simulation was run and the computed ATA flow and pressure waveforms were used to calculate values of R^{comp}_{TOT} and C^{comp}_{TOT}. If the discrepancy between these computed values and experimentally determined R_{TOT} and C_{TOT} was larger than 4%, further iterations were made for R^i_{prox}, R^i_{dist} and C^i for all branches. The relation between the parameters of all Windkessel models and the values of resistance and compliance of the entire peripheral vasculature ($R_{peripheral}$, $C_{peripheral}$) is

$$\frac{1}{R_{peripheral}} = \sum_i \frac{1}{R^i}, \quad C_{peripheral} = \sum_i C^i.$$

Knowledge of R_{TOT}, C_{TOT}, $R_{peripheral}$ and $C_{peripheral}$ allows one to compute $R_{central}$, $C_{central}$ for each specimen. Lastly, the following regional flow distributions were targeted: 17% of CO to the innominate artery, 10% to the left carotid and 17% to the IAA [25,26].

(c) Statistical analysis

Computed results are presented as mean ± s.e.m. One-way ANOVA was used to assess differences among the four groups. *Post hoc* pairwise comparisons were performed using the

Benjamini–Hochberg correction method, with $p < 0.05$ considered significant. All analyses were performed using the open source statistical software R.

(d) Pulse wave velocity analysis

PWV was calculated as the ratio of the centreline distance between two locations of interest and the corresponding pressure pulse transit time. The transit time was measured using an 'intersecting tangent algorithm' that defines the foot of a pressure waveform as the intersection between the horizontal tangent intersecting its diastolic minimum and the tangent to the maximum systolic gradient [27]. Three commonly used *PWV* metrics were compared: left carotid to iliac artery (CCA–iliac), ascending thoracic aorta to infrarenal abdominal aorta (ATA–IAA) and ascending thoracic aorta to iliac artery (ATA–iliac).

3. Results

For the purposes of illustration, figure 5 summarizes the results of computed local (cyclic pressure and flow) and global (*PWV*) haemodynamics based on anatomical models endowed with mouse-specific regional biaxial tissue properties for four representative mice: one male and one female WT (left, grey waveforms and bar plots) and one male and one female KO (right, black waveforms and bar plots). Mouse- and region-specific values of circumferential and axial material stiffness and wall thickness are shown in the centre of the figure. The actual computational domains are shown only for WT_F1 and KO_F1, but recall that figure 2 shows all 11 anatomical models. In general, the KO mice exhibited marked increases in aortic length and tortuosity, especially in the ATA and DTA. Figure 5 reveals further that, while there are no marked differences in circumferential material stiffness $\mathscr{C}_{\theta\theta}$ between these WT and KO mice, there is an overall increase in thickness h in KO compared with WT for both sexes and thus increased structural stiffness. Nonetheless, circumferential material stiffness is largest at the pDTA (location C) and smallest at the infrarenal aorta (location F) for all four mice used in this comparison; the axial material stiffness $\mathscr{C}_{ZZ}$ is largest at the pDTA (location C) but smallest at the ATA (location B). Computed flow and pressure waveforms are shown on the left and right sides of the figure. While the WT male has a larger CO than its female counterpart, CO is similar between these male and female KOs. The KO mice also show increased central pulse pressure (cPP) for both sexes: 35 versus 48 mmHg for WT and KO males and 32 versus 53 mmHg for WT and KO females. The differences in pulse pressure (PP) between WT and KO mice diminish in the distal part of the aorta, where values are comparable across genotypes for both male (30 versus 25 mmHg) and female (28 versus 31 mmHg) mice. As examples, the figure also shows the pressure pulse transit time between the ATA and IAA for the males. ATA–IAA *PWV* is larger for these KO mice, with a more substantial increase for females (4.47 versus 3.16 $\mathrm{m\,s^{-1}}$) than for males (4.03 $\mathrm{m\,s^{-1}}$ versus 3.85 $\mathrm{m\,s^{-1}}$). In the following, we summarize the results for global haemodynamics, regional geometry, wall mechanics and haemodynamics, and *PWV* for all mice constituting all four groups.

(a) Global haemodynamics

Table 1 lists mouse-specific values of adjusted CO, R_{TOT}, C_{TOT} that were assigned to each specimen of the anatomy cohort via allometric scaling. WT males have a statistically higher CO than the other groups. Females have a statistically significantly higher R_{TOT} and lower C_{TOT} than males. Figure 3*a* seems to suggest that KO_F exhibit a negative trend between CO and body mass, but subjects in this group display little variability in body mass. The WT_F group shows a steep increase in both R_{TOT} and C_{TOT} with body mass.

Figure 6*a* separates R_{TOT} into central (R_{central}, in red) and peripheral ($R_{\mathrm{peripheral}}$, in blue) components. $R_{\mathrm{peripheral}}$ accounts for more than 80% of the total vasculature resistance for all four groups. R_{TOT} and $R_{\mathrm{peripheral}}$ are statistically higher in females than in males of the same genotype. R_{central} is higher in the KO than in WT of the same sex, which is consistent with the

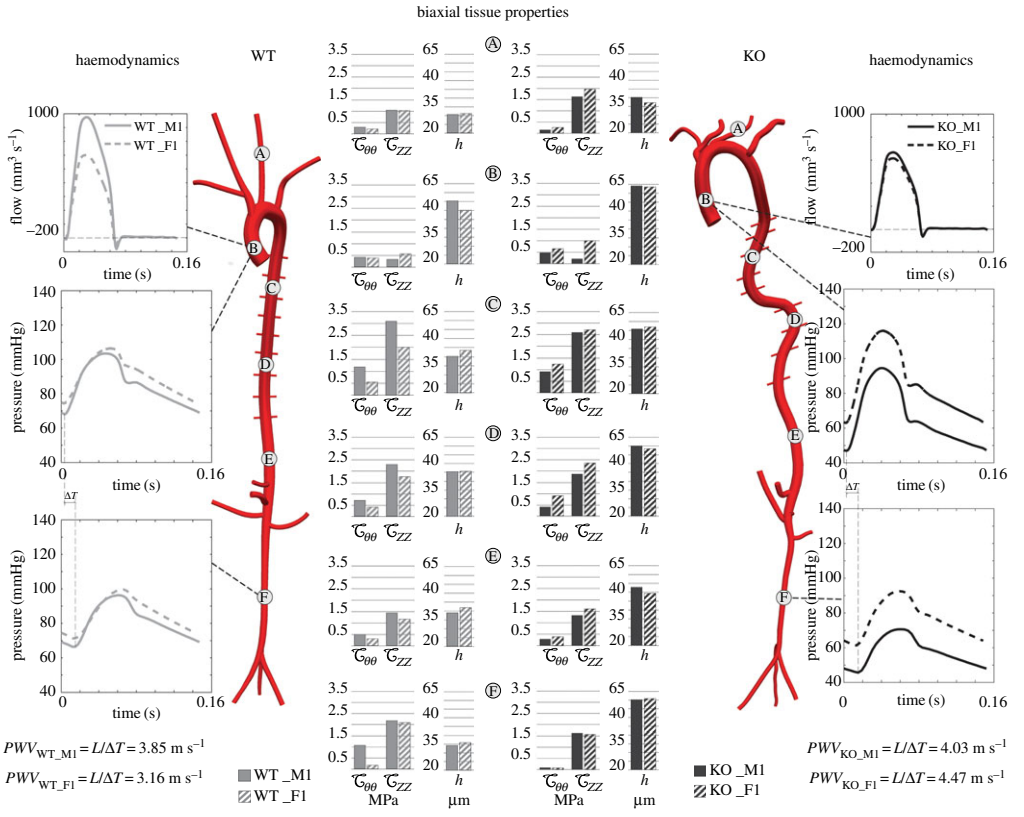

Figure 5. Computed global and local haemodynamics based on mouse-specific geometric models (two micro-CT models shown for illustrative purposes, WT_F1 and KO_F1) and mouse-specific biaxial tissue properties (biaxial material stiffness and wall thickness) for four representative subjects: WT_M1 and WT_F1 on the left and KO_M1 and KO_F1 on the right. Additional mouse-specific values are in the electronic supplementary material, table S1. (Online version in colour.)

smaller radii and increased tortuosity in the KO. Figure 6*b* separates C_{TOT} into central ($C_{central}$, in red) and peripheral ($C_{peripheral}$, in blue) components. C_{TOT} is smaller in the KO males and females (statistically only for the males), in part because of the increase in structural stiffness and decrease in radii, which result in smaller cyclic strains. C_{TOT} is statistically smaller in the female than in the male of the same genotype. Surprisingly, $C_{peripheral}$ accounts for more than 70% of the total compliance for all groups except WT female. Numerical values are reported in the electronic supplementary material, table S3 and S4.

We also compared experimental and computed pressures within the ATA for each group (figure 7). The computed pressure decay and PP match well the experimental data. We observe a larger variability in the experimental data than in the computed results, in part because of a wider range of body mass in the haemodynamics cohort than in the anatomy cohort. For WT_M, body mass ranged between 20 and 50 g for the haemodynamics cohort versus 33–38 g for the anatomy cohort. For the remaining groups, the ranges in body mass for the haemodynamics and anatomy cohorts were: 24–39 versus 30–31 g for KO_M; 22–31 versus 23–27 g for WT_F; and 25–29 versus 24–25 g for KO_F. The WT_F group showed the largest variability in the computed pressure owing to the stronger dependence of R_{TOT} and C_{TOT} with respect to body mass, as noted above. Specific values of computed systolic (P_{SYS}), mean (P_{MEAN}), diastolic (P_{DIAS}) and central pulse (cPP) pressures are listed in the table embedded in figure 7. There is an increase in cPP in KO groups compared with WT in males and females, though with a fundamental difference: diastolic pressure decreases in the males but systolic pressure increases in the females. Our computational

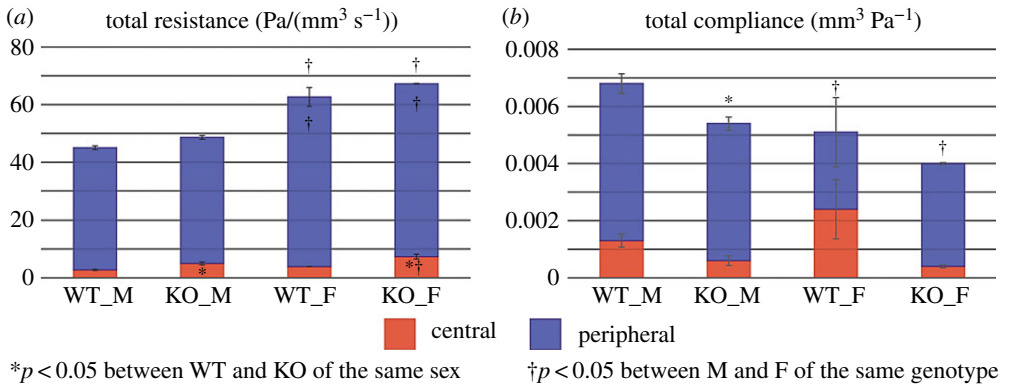

Figure 6. Separation of R_{TOT} (*a*) and C_{TOT} (*b*) into central (red) and peripheral (blue) components for all four groups.

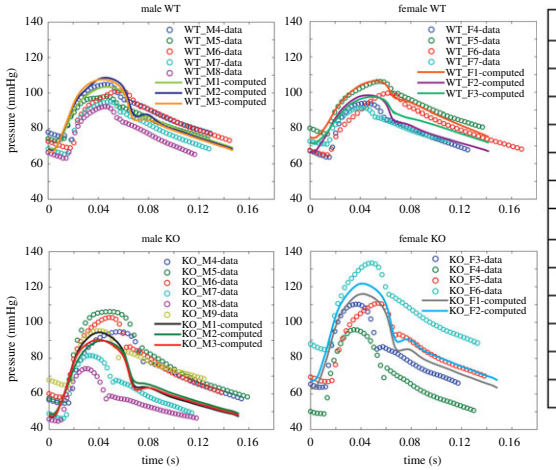

WT_M					WT_F				
mouse	P_{MEAN}	P_{SYS}	P_{DIAS}	cPP	mouse	P_{MEAN}	P_{SYS}	P_{DIAS}	cPP
WT_M1	80	103	68	35	WT_F1	85	106	74	32
WT_M2	81	109	67	41	WT_F2	77	98	67	32
WT_M3	80	108	67	41	WT_F3	80	97	71	26
mean	80	107	67	39	mean	81	101	71	30[a]
s.d.	1	3	1	3	s.d.	4	5	4	3
KO_M					**KO_F**				
mouse	P_{MEAN}	P_{SYS}	P_{DIAS}	cPP	mouse	P_{MEAN}	P_{SYS}	P_{DIAS}	cPP
KO_M1	63	95	47	48	KO_F1	81	116	63	53
KO_M2	62	90	49	41	KO_F2	85	122	67	54
KO_M3	62	90	47	43	-	-	-	-	-
mean	62[b]	92[b]	48[b]	44	mean	83[a]	119	65[ab]	51[ab]
s.d.	1	3	1	3	s.d.	3	4	3	1

[a]$p < 0.05$ between M and F of the same genotype
[b]$p < 0.05$ between WT and KO of the same sex

Figure 7. Comparison of experimental (circles) and computed (solid lines) pressure waveforms within the ATA (section B in figure 5) for all four groups ($n = 4$ or 5 mice per haemodynamics cohort, $n = 2$ or 3 per anatomy cohort). The embedded table lists values of computed mean (P_{MEAN}), systolic (P_{SYS}), diastolic (P_{DIAS}) and central pulse (cPP) pressures within the ATA. All values are reported in mmHg. We aimed to reproduce murine haemodynamics under anaesthesia. Notice the greater specimen-to-specimen variation in KO than in WT mice, independent of sex.

simulations captured the same behaviour. Male WT have higher cPP than females; conversely, female KO have higher cPP and P_{MEAN} than males. Finally, note that the Reynolds number in our simulations ranged from $Re = 611$ in the ATA at peak systole to $Re = 0.6$ in the intercostal arteries at diastole.

(b) Regional wall mechanics, haemodynamics and inner diameter data

Figure 8 illustrates P_{MEAN}, PP, structural stiffness ($\mathscr{C}_{\theta\theta}{}^{*}h$), material stiffness ($\mathscr{C}_{\theta\theta}$), wall thickness ($h$) and internal diameter (id) along the aorta and CCA for the WT (grey bar) and KO (black bar) groups. Numerical values are reported in figure 7 and the electronic supplementary material, tables S1, S5 and S6. P_{MEAN} is the time average of the computed pressure at the locations of interest and it drops along the aorta as expected: male WT and KO have a comparable drop in P_{MEAN} from the ATA to the iliac artery (9 and 10 mmHg, respectively) while female WT have a smaller drop in P_{MEAN} than the female KO (10 and 16 mmHg, respectively). KO males have statistically smaller P_{MEAN} than WT males and KO females at all locations. Bar plots of the

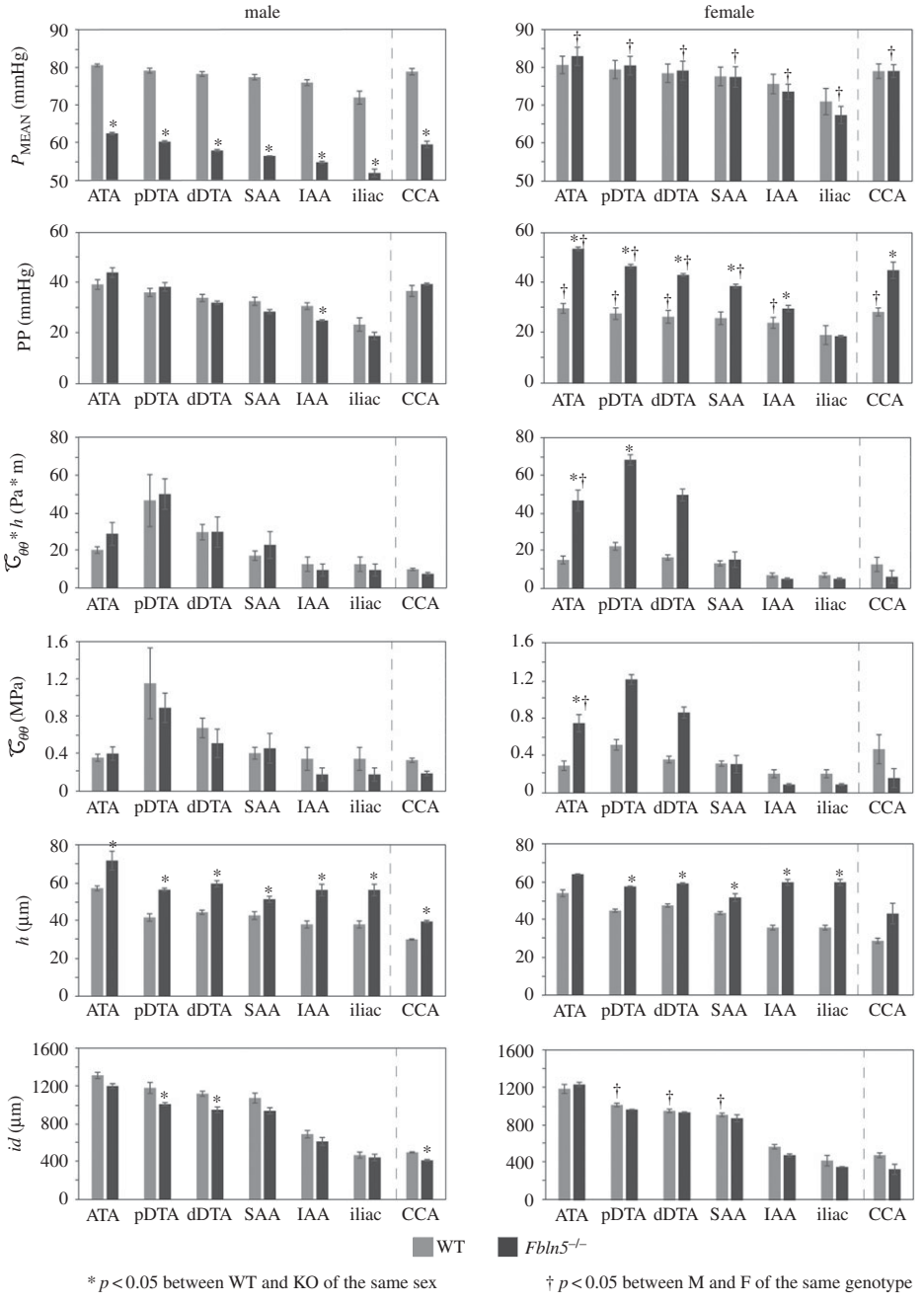

Figure 8. Regional values (mean ± s.e.m.) of mean blood pressure (P_{MEAN}), pulse pressure (PP), structural stiffness ($\mathscr{C}_{\theta\theta} * h$), circumferential material stiffness ($\mathscr{C}_{\theta\theta}$), wall thickness ($h$), and internal diameter (id) for male and female WT (grey bars) and KO (black bars) mice.

distribution of computed PP reveal an attenuation of the pulse along the aorta in all four groups. As noted earlier, male and especially female KOs have higher PP than their WT counterparts in the proximal part of the aorta: WT and KO have ATA PP of 39 versus 44 mmHg, respectively, for the male and 30 versus 54 mmHg, respectively, for the female. Differences in PP between WT and KO mice diminish in the distal part of the aorta. Iliac artery PP is slightly larger in the WT than in the KO in males (23 versus 19 mmHg) but identical for the females (19 versus 19 mmHg). KO

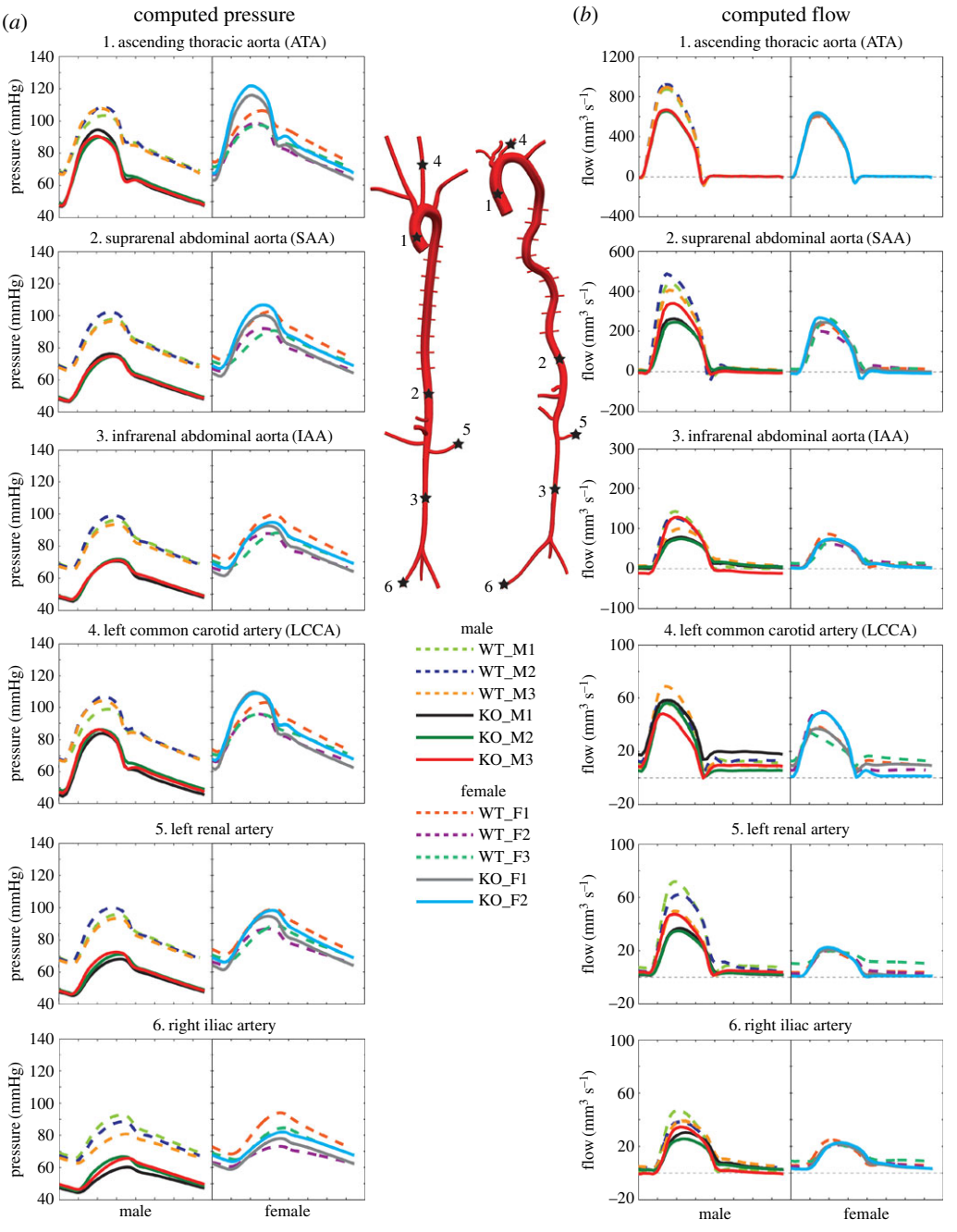

Figure 9. Computed pressure (*a*) and flow (*b*) waveforms for WT (dashed lines; for example, left anatomical model) versus KO (solid lines; for example, right anatomical model) for both males (first column) and females (second column) at six different locations: 1. ascending thoracic aorta (ATA), 2. suprarenal abdominal aorta (SAA), 3. infrarenal abdominal aorta (IAA), 4. left common carotid artery (LCCA), 5. left renal artery and 6. right iliac artery.

females have statistically higher PP than KO males and WT females at all locations except the iliac artery.

Mouse-specific values of $\mathscr{C}_{\theta\theta}$ and h were determined from experimental data on wall mechanics and assigned to the different locations along the arterial tree, as explained in §2b(ii). All four groups have a similar distribution of $\mathscr{C}_{\theta\theta}{*}h$ along the aorta: a peak value at the pDTA

Table 2. Values of aortic length (*L*) in mm, aortic pulse transit time (PTT) in ms, and pulse wave velocity (*PWV*) in m s^{-1}, from left carotid to iliac artery (CCA–iliac), from aortic root to infrarenal abdominal aorta (ATA–IAA) and from aortic root to iliac bifurcation (ATA–iliac) for all four groups.

		wild-type_male (WT_M)					wild-type_female (WT_M)				
		WT_M1	WT_M2	WT_M3	mean	s.d.	WT_F1	WT_F2	WT_F3	mean	s.d.
L	CCA–iliac	56.2	55.9	51.6	54.6	2.5	50.8	51.9	37.0	46.6	8.3
	ATA–IAA	42.7	44.5	43.2	43.5	0.9	38.5	40.0	42.6	40.3[a]	2.0
	ATA–iliac	52.2	55.2	53.5	53.6	1.5	48.4	52.3	55.0	51.9	3.3
PTT	CCA–iliac	9.7	12.2	14.9	12.3	2.6	14.7	15.7	20.9	17.1	3.3
	ATA–IAA	11.1	10.9	12.0	11.3	0.6	12.2	11.9	17.8	14.0	3.3
	ATA–iliac	13.6	14.3	16.9	14.9	1.7	19.6	18.3	23.8	20.6	2.9
PWV	CCA–iliac	5.8	4.6	3.5	4.6	1.2	3.5	3.3	1.8	2.8	0.9
	ATA–IAA	3.9	4.1	3.6	3.8	0.2	3.2	3.4	2.4	3.0	0.5
	ATA–iliac	3.8	3.9	3.2	3.6	0.04	2.5	2.9	2.3	2.5[a]	0.3
		knockout_male (KO_M)					knockout_female (KO_F)				
		KO_M1	KO_M2	KO_M3	mean	s.d.	KO_F1	KO_F2	—	mean	s.d.
L	CCA–iliac	59.0	51.6	62.8	57.8	5.7	62.9	60.3	—	61.6	1.8
	ATA–IAA	49.2	49.4	51.8	50.1[b]	1.4	50.1	49.5	—	49.8[b]	0.5
	ATA–iliac	60.4	58.6	64.3	61.1[b]	2.9	61.0	61.2	—	61.1[b]	0.1
PTT	CCA–iliac	14.9	12.6	16.2	14.6	1.8	15.9	15.4	—	15.7	0.4
	ATA–IAA	12.2	13.0	10.5	11.9	1.3	11.2	13.7	—	12.5	1.8
	ATA–iliac	17.2	15.0	17.8	16.7	1.5	18.2	20.5	—	19.4	1.6
PWV	CCA–iliac	4.0	4.1	3.9	4.0	0.1	4.0	3.9	—	3.9	0.0
	ATA–IAA	4.0	3.8	4.9	4.3	0.6	4.5	3.6	—	4.0	0.6
	ATA–iliac	3.5	3.9	3.6	3.7	0.2	3.4	3.0	—	3.2	0.3

[a] $p < 0.05$ between M and F of the same genotype.
[b] $p < 0.05$ between WT and KO of the same sex.

and a gradual decrease in the distal part of the aorta with the smallest values at the IAA and iliac artery. KO groups exhibit higher $\mathscr{C}_{\theta\theta}{}^{*}h$ than WT in the proximal aorta but an opposite trend at the IAA, iliac, and carotid artery for both males and females. Furthermore, males have overall higher $\mathscr{C}_{\theta\theta}{}^{*}h$ than females for the WT groups; conversely, females have higher $\mathscr{C}_{\theta\theta}{}^{*}h$ than males in the KO. $\mathscr{C}_{\theta\theta}$ have a similar distribution to $\mathscr{C}_{\theta\theta}{}^{*}h$ along the aorta for all four groups. For the males, WT and KO alternate higher values between the two groups at different locations. KO females exhibit higher values in the proximal part of the aorta and lower values in the distal part than WT. KO females have statistically higher $\mathscr{C}_{\theta\theta}{}^{*}h$ and $\mathscr{C}_{\theta\theta}$ at the ATA than WT female and KO male. Wall thickness h shows a marked increase for the KO groups compared with WT along the entire aorta for both males and females. The higher values of h in the KO groups are statistically significant at all locations except at the ATA and CCA for the females. *Id* values were extracted from the anatomy reconstructed from the micro-CT data as explained in §2b(i). *Id* is overall smaller in KO than in WT mice. Electronic supplementary material, figure S1 further compares experimental and computed values of diameter distension $(d_{\text{systole}} - d_{\text{diastole}})/d_{\text{diastole}}$ at the ATA, SAA, IAA and CCA for each group.

Figure 9 shows computed pressure (*a*) and flow (*b*) waveforms for WT (dashed line) and KO (solid line) males (left column) and females (right column) at six different locations: ATA, SAA, IAA, left CCA, left renal artery and right iliac artery. Visualization of the pressure waveforms

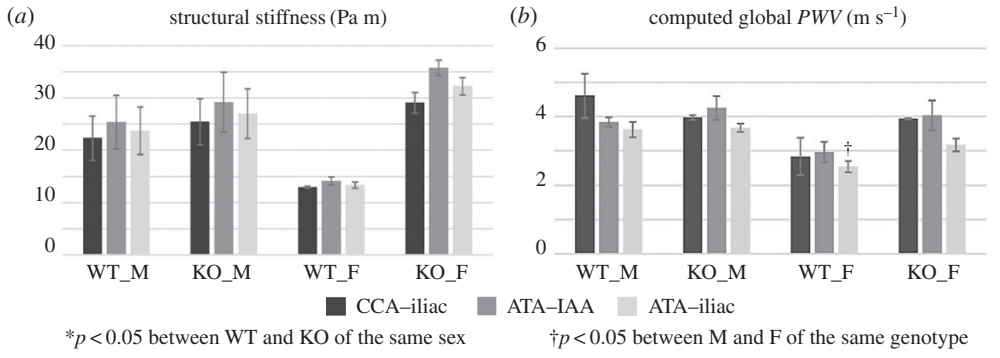

Figure 10. Values (mean ± s.e.m.) of measured structural stiffness (*a*) and computed *PWV* (*b*) for all four groups. Both quantities are calculated for three different portions of the arterial tree: left common carotid artery to iliac artery (CCA–iliac), ascending thoracic aorta to infrarenal abdominal aorta (ATA–IAA) and ascending thoracic aorta to iliac artery (ATA–iliac).

shows qualitatively similar details as discussed above, but we observe further the different specimens instead of just mean values analysed in figure 8. Results from figure 8 are again evident: KO males exhibit lower P_{MEAN} than WT, while the WT and KO females have comparable P_{MEAN}. KO models have an augmented cPP (for both male and especially female) compared with WT. The PP decreases down the length of the murine aorta and there are no differences in PP between WT and KO at the IAA. In the renal artery, WT and KO males have a PP of 31 and 24 mmHg, respectively, while WT and KO females have a PP of 24 and 32 mmHg, respectively. There are no substantial differences in flow waveforms between WT and KO even though male WT have higher CO. There is a good qualitative agreement between our computed flow waveform and the velocity reported by Hartley *et al.* [28]. We can observe backflow in the ATA and SAA, but not in the IAA, CCA and renal arteries.

(c) Computed pulse wave velocity

We calculated three different commonly used values of *PWV*: CCA–iliac, ATA–IAA and ATA–iliac; specific values are in table 2 along with path length and computed transit time. In figure 10, we compare values of computed *PWV* with corresponding values of spatially averaged structural stiffness (i.e. a weighted mean within the segments of interests, considering the length of each segment as a weight). KO groups tend to have higher structural stiffness than WT groups of the same sex. WT males have higher structural stiffness than WT females; conversely, KO males have lower structural stiffness than KO females. Computed *PWV* does not follow the same trends as structural stiffness. CCA–iliac stiffness increases by 14% from WT to KO in males but the associated *PWV* decreases by 14%. A 14% increase for ATA–iliac stiffness results in only a 2% increase in *PWV*. Furthermore, the higher values of structural stiffness of KO females compared with KO males is not captured by any of the *PWV* metrics. *PWV* depends on many factors, including arterial properties, geometries, and flow as well as perivascular support. Furthermore, we found that heterogeneity of the structural stiffness of the arterial wall contributes to changes in the measured *PWV* [29–33]. More details are shown in the electronic supplementary material, table S7.

4. Discussion

Central artery stiffening plays critical roles in dictating both the local wall mechanics/mechanobiology and the global haemodynamics/pathophysiology [34], which is particularly important because local and global effects appear to relate within a potentially insidious positive feedback loop [35]. Computational FSI studies can thus contribute significantly to our

understanding of these complex, clinically important feedback loops. We previously presented FSI simulations for the human central vasculature [7] using the best data available in the literature on age-dependent (30, 40, 60 and 75 years old) regional variations in aortic properties [6]. Results were generally consistent with clinical findings, including age-associated increases in *PWV* and cPP. Importantly, we also quantified progressive age-related reductions in elastic energy stored during a cardiac cycle, which relates to local biomechanical functionality. Limitations, however, included a lack of complete data on young healthy subjects as well as a lack of detailed anatomic changes with ageing—we increased luminal diameters and axial lengths numerically based on reported trends.

As noted earlier, murine data offer some advantages over human data for informing FSI computations, particularly given the ability to study diverse mouse models (genetic, pharmacologic and surgical) representing myriad conditions. One of the key contributions of this study, therefore, is development of FSI models for adult male and female WT controls (C57BL/6 × 129/SvEv) under anaesthetized conditions to which results from other models can be compared. Importantly, Bellini *et al.* [36] recently showed for the ATA that biomechanical properties are similar across multiple mouse models used as controls (including C57BL/6 and C57BL/6 × 129/SvEv), hence the present results are likely to be broadly representative of WT controls.

In addition to the WT group, we also developed FSI models of the adult fibulin-5 null (*Fbln5*$^{-/-}$ or KO) mouse model, which represents a stable model of early vascular ageing given its loss of elastic fibre integrity [12]. Despite prior studies of mechanical properties [13] and basic cardiovascular function [37] in fibulin-5 null mice, we present the first detailed FSI simulations for this important mouse model. Both WT and KO groups were further divided by sex. Although chronological age was consistent across the four groups, the variability within the KO groups may have resulted from different degrees of elastopathy, which is to say that responses to a genetic mutation need not progress the same as different mice age. It will also be interesting to compare results from WT and *Fbln5*$^{-/-}$ mice with similar calculations for naturally aged mice, but this was beyond the current scope. In particular, although the structural integrity of the elastic fibres and laminae appears to be largely preserved in aged murine vessels, the age-related increase in collagen and glycosaminoglycans necessarily reduces the per cent elastin within the wall [38,39]. Hence, energy storage and distensibility are reduced in ageing and cases of elastopathy, but for different reasons.

Although longitudinal data can be collected non-invasively in mice (e.g. micro-CT and ultrasound), associated information on biaxial wall properties, thickness and histological composition require terminal procedures. Hence, typically not all data can be collected from a single mouse. A key methodological contribution of this paper is development of a workflow to integrate *in vivo* and *in vitro* experimental data on haemodynamics, wall mechanics and anatomy from multiple cohorts into single 'mouse-specific' computational models of vascular biomechanics. Indeed, because haemodynamic conditions can even be influenced strongly by differences in anaesthetic depth from imaging session to imaging session, the ability to normalize results by body mass can decrease inherent variability in measurements within and across subjects. We thus developed a methodology to assign mouse-specific haemodynamic data to micro-CT based models of the central vasculature using body mass based allometric scaling of quantities such as CO, R_{TOT} and C_{TOT}. Local values of biaxial material stiffness and wall thickness can also be assigned in a mouse-specific manner, with associated linear interpolations as needed.

(a) Biomechanical characteristics

Information obtained from calibrated computational groups yields the following advantages relative to the experimental data from which it is derived: (i) insights can be gleaned for quantities not easily accessible through experiments, such as pressure indices at the level of the renal arteries or values of peripheral resistance and compliance for different genotypes and sexes; (ii) a high-resolution description of quantities such as *PWV*, which further enables interpretation of complex

interdependencies among these quantities and spatial variations in stiffness and anatomy. In the following paragraphs, we summarize statistically significant differences in haemodynamics and biomechanics for the different groups.

Sex differences

- WT mice: Males have larger body mass and higher CO than females, but P_{MEAN} is comparable between males and females (which suggests that R_{TOT} is smaller in males). Males also show smaller $R_{peripheral}$, larger C_{TOT} and higher PP within the ATA, pDTA, dDTA, IAA and CCA. Females have smaller *id* at pDTA, dDTA and SAA. ATA–IAA length and ATA–iliac *PWV* is larger in the males.
- Fibulin-5 null mice*:* Females have smaller body mass and larger R_{TOT}, $R_{peripheral}$, $R_{central}$ and P_{MEAN} than males though CO is comparable between the two groups. Conversely, C_{TOT} is larger in the males. Females have larger pressure indices ($P_{MEAN,}$ $P_{SYS,}$ P_{DIAS} and cPP) in the ATA than males. Lastly, females have larger material and structural stiffness in the ATA.

Genotype differences

- Male*:* KO_M mice have lower body mass, CO and C_{TOT} than WT. KO mice have higher $R_{central}$ than WT. Within the ATA, the KO mice have lower values of P_{MEAN}, P_{SYS} and P_{DIAS}. The KO mice also have lower P_{MEAN} at all other locations along the aorta as well as in the CCA and lower PP at IAA. The KOs also have an overall larger thickness *h* and smaller *id* within the pDTA, dDTA and CCA, which explains higher $R_{central.}$ KOs have greater ATA–IAA and ATA–iliac centreline lengths.
- Female*:* The KO_F mice have larger $R_{central}$ than the WT, owing to increased tortuosity. The KO mice also have higher P_{SYS}, P_{DIAS} and cPP within the ATA and higher PP at all other locations except the IAA. The KOs have higher material and structural stiffness at the ATA and higher structural stiffness at pDTA. Thickness *h* is larger in the KO at all locations except for ATA and CCA. KOs have greater ATA–IAA and ATA–iliac centreline lengths.

The following indices, although not reflecting statistically significant differences owing to the small number of samples, are also worth noting. (i) Both male and female KO groups have higher structural stiffness in the proximal part of the aorta than WT of the same sex. Conversely, KO groups have lower structural stiffness in the distal part of the aorta (namely, IAA and iliac artery). These differences result in higher PP in the proximal part of the aorta in the KO groups than in WT and lower (for males) or comparable (for females) PP distally. These findings suggest a greater loss of functionality in the proximal aorta with loss of elastic fibre integrity compared with the distal part, consistent with the expected differential elastin–collagen ratios in normalcy. (ii) The increase in cPP in the KO groups seems to follow two different mechanisms in the male and female mice. cPP increases in the males mainly because of a decrease in diastolic pressure associated with a larger stiffness and lower CO. Conversely, cPP increases in the females mainly because of an increase in systolic pressure associated with a larger stiffness and maintained CO. These computational trends reflect the experimental data. (iii) The distribution of total compliance between central and peripheral components revealed that WT_F are the only group in which $C_{central}$ accounts for more than 50% of the total compliance. This finding suggests that healthy females have larger aortic compliance than healthy males and thus could exhibit different responses during the progression of certain cardiovascular diseases.

Differently from what we observe in humans [40], $C_{peripheral}$ accounted for more than 70% of the total compliance in all the other groups. From physiological and biomechanical perspectives, there are clearly fundamental differences between the human and murine cardiovascular systems. For example, mice have a much faster heart rate, much smaller dimensions, lower Reynolds

and Womersley numbers, and, most critically for our purposes, a different distribution of aortic stiffness and pulse amplification along the aorta than humans. Moreover, species with faster heart rates exhibit higher arterial elastin–collagen ratios and higher *in vivo* axial stretches [41]. The mouse aorta also has significant contractile capability, which is less expected in the human, though contractility was not modelled directly owing to the expected lower extent under anaesthesia but also a general lack of information on *in vivo* values. These differences might help explain our reported distribution of compliance, noting that the anaesthesia could contribute further to an overestimation of the total compliance, which in turn could explain the large estimates of peripheral compliance. Figure 4 illustrates this point: whereas the time constant τ is set directly by fitting an exponential decay to the diastolic portion of the aortic waveform, and contributes to C_{TOT}, an underestimation of the total resistance R_{TOT} from the CO and mean pressure, which is lower under anaesthesia, would necessarily lead to an overestimation of the total compliance C_{TOT}. This issue must certainly be investigated further, but it is beyond the current scope to perform a detailed comparison across species.

(b) Pulse wave velocity

We compared three computed metrics of *PWV* (CCA–iliac, ATA–IAA and ATA–iliac) with the corresponding spatial averages of structural stiffness. We observed that *PWV* does not always capture regional differences or changes in stiffness, which is often a key manifestation of vascular disease. Specific examples of these discrepancies are as follows.

Sex differences

— Fibulin-5 null mice: Although the females have a greater average aortic structural stiffness, all three *PWV* metrics were lower in females than in males. This difference is due to the complex interdependence of *PWV* on geometry, stiffness and flow. We also found that regional differences in structural stiffness impacts the measured *PWV*, specifically greater heterogeneity results in lower *PWV*.

Genotype differences

— Male mice: CCA–iliac stiffness was larger in the KOs than in WTs while the *PWV* was less. In addition to the previously discussed impact of spatial stiffness heterogeneity on *PWV*, it is worth noting that no physical pulse travels between the CCA and the iliac, adding complexity to the interpretation of this index.

To validate our computational findings on *PWV*, we estimated the experimental *PWV* from the available data. Using the Doppler velocity measured in the ATA and IAA, we estimated the pulse transit time in each mouse of the haemodynamics cohort using a foot-to-foot algorithm. Centreline aortic length was then measured from the micro-CT cohort to estimate the experimental *PWV*. Mean values of experimental ATA–IAA *PWV* are (in $\mathrm{m\,s^{-1}}$): 3.5 ± 0.2 for WT_M and 3.9 ± 1.2 for WT_F, 5.9 ± 0.6 for KO_M and 4.7 ± 0.4 for KO_F. Our computational values (table 2) are thus similar to those from the experimental data. Specifically, larger values of ATA–IAA *PWV* are observed in both KO groups. Our *PWV* values also agree with those reported in the literature by Hartley *et al.* [42], who reported aortic *PWV* of $3.79 \pm 0.1\,\mathrm{m\,s^{-1}}$ in 10 WT C57BL/6J mice at 13 months of age.

(c) Comparison with prior work

Notwithstanding prior computational fluid dynamics studies (i.e. haemodynamics in the presence of rigid walls) in mice (e.g. [25,26,43,44]), to the best of our knowledge there have been few mouse-specific three-dimensional FSI models of central haemodynamics besides our

prior study of the effects of catheter size on murine haemodynamics [18]. Trachet and colleagues [45] studied abdominal aortic flows in angiotensin II-infused mice to gain insight into the preferential occurrence of dissection in the suprarenal aorta while De Wilde and colleagues [46] studied the effects of anaesthesia, rest and exercise on haemodynamics in the carotid artery. Because both of these excellent studies focused on local regions, the arterial wall properties (modelled using an isotropic Arruda–Boyce model) were assumed to be spatially uniform, with wall thickness assumed to be 10% of the local radius. These models also relied on *in vivo* measurements of velocity and geometry assessed in a representative animal. Owing to the impracticality of collecting multiple types of biomechanical data from the same animal, these studies did not include pressure waveforms from the same subject. Our 11 models, in contrast, were built on regional *in vitro* biaxial mechanical testing as well as *in vivo* ultrasound and pressure measurements for groups of approximately five mice for each of the four groups: WT_M, WT_F, KO_M and KO_F. There are, therefore, no results with which we can compare directly. Note, however, that Aslanidou *et al.* [47] developed a one-dimensional model of the anaesthetized murine cardiovascular system based on micro-CT images of male WT C57BL/6J and $ApoE^{-/-}$ mice (12–15 weeks old) and literature data. This model included 85 arterial segments and was validated against catheter-based pressure and ultrasound-based diameter and velocity waveforms. Our WT_M results compare well with their findings, as, for example, 15 versus 14 ml min^{-1} for CO and 3.8 versus 4.4 m s^{-1} for ATA–IAA *PWV*, respectively. Our ATA P_{MEAN} was lower (80 versus 98 mmHg, which could reflect different levels of anaesthesia), but we observed a similar 4 mmHg drop in P_{MEAN} from the ATA to the IAA. Our computed value of PP in the ATA was similar (39 versus 41.7 mmHg), but there was a substantial difference in drop in PP from the ATA to the IAA (8 mmHg in our study versus 1.5 mmHg in the study by Aslanidou and colleagues). Finally, our values for R_{TOT} and C_{TOT} for the WT_M are similar to those reported by Segers *et al.* [48], who fitted a four-element Windkessel model to experimental data ($R_{TOT} = 54.66 \pm 17.33$ versus our $R_{TOT} = 45.0 \pm 0.5$ Pa/(mm^3 s^{-1})), and $C_{TOT} = 0.00375 \pm 0.00113$ mm^3 Pa^{-1} versus our $C_{TOT} = 0.0068 \pm 0.0001$ mm^3 Pa^{-1}). Our value of $C_{central}$ (0.0013 ± 0.0002) in the WT_M group compared well with that reported by Guo & Kassab [49] (0.002 mm^3 Pa^{-1}), who studied the relationship of $C = \Delta V / \Delta P$ for the aorta and its main branches including the iliac bifurcation.

(d) Limitations

Nevertheless, our model, like all others, remains to be improved. Biaxial material properties were measured in only five central arteries; additional measurements in vessels such as the subclavians, iliacs and mesenterics should be considered in the future. Albeit measured *in vitro*, the extreme axial extensibility of the ATA was not captured by our FSI model, thus changes in ATA volume during systole are likely to be underestimated. This limitation could lead to an underestimation of the axial compliance of the ATA, a key contributor to $C_{central}$, which in turn could lead to a larger cPP. Because of biaxial coupling of wall mechanics, this issue could also help explain discrepancies between experimental and computed values of diameter distension at the ATA as shown in the electronic supplementary material, figure S1.

Our model also does not account for the Fåhræus–Lindqvist effect, which describes a significant decrease in the apparent blood viscosity in vessels of diameters less than 300 µm [50]. The intercostal arteries of our models have a diameter of 170 µm and the renal and tail arteries of two WT female models have a diameter slightly smaller than 300 µm. In these locations the higher viscosity considered likely resulted in slightly higher values of both mean flow and mean pressure (cf. [47]), with no significant effects on the outlet boundary conditions and thus overall results.

5. Conclusion

We presented a new workflow for studying mouse-specific haemodynamics in the central vasculature including FSI and regionally varying biaxial arterial wall properties. Results for adult

WT mice should serve as important controls for many future studies involving diverse genetic, pharmacological and surgical mouse models. In addition, we studied an important mouse model ($Fbln5^{-/-}$) of early vascular ageing due to a marked elastopathy and as a function of sex. Increased structural stiffness of the proximal central arteries in fibulin-5 deficiency, due largely to increased wall thickness and collagen–elastin ratios, led to increases in cPP and *PWV* in both male and female mice. This increased *PWV* did not reflect well the underlying regional differences in stiffness, however, thus suggesting that this spatially averaged measure is not sensitive to local changes *per se*, particularly when comparing results between males and females.

Ethics. All animal procedures were approved by the Institutional Animal Care and Use Committee (IACUC) of Yale University, New Haven, CT, USA.

Data accessibility. The haemodynamics computational framework CRIMSON [15] employed to run the FSI simulations can be downloaded at http://www.crimson.software. The CRIMSON files for each of the ($n = 11$) subjects of the anatomy group have been uploaded to a Dryad open source repository: http://dx.doi.org/10.5061/dryad.64c32m5 [51]. These files contain micro-CT data, CAD segmentations of the aorta and main branches, biaxial tissue properties, inflow waveform, and adapted finite-element mesh. A table with the full list of Windkessel values can also be found in the repository.

Authors' contributions. F.C. contributed to the development of a workflow for melding experimental data collected in three different animal cohorts to inform a single computational model, then ran the FSI computations, analysed the results and drafted the manuscript; J.F. carried out all the experimental analyses on mice and analysed the results; P.A. built the three-dimensional anatomies from micro-CT image data; C.L. contributed to setting up the computational models using the CRIMSON framework; Z.W.Z. collected the micro-CT image data; J.D.H. jointly conceived and coordinated the study, supervised the experimental work and drafted the manuscript; C.A.F. jointly conceived and coordinated the study, supervised the computational analyses and drafted the manuscript. All authors gave final approval for publication.

Competing interests. We do not have any competing interests.

Funding. This work was supported, in part, by grants from the NIH (R01 HL105297, P01 HL134605), by the European Research Council Starting grant no. 307532 and by the Edward B. Diethrich M.D. Professorship. Additional computing resources were provided by the NSF via grant no. 1531752 MRI: Acquisition of Conflux, A Novel Platform for Data-Driven Computational Physics (Tech. Monitor: Ed Walker).

Acknowledgements. The authors wish to acknowledge Simmetrix, Inc. for its MeshSim mesh generation library and Dr Vasilina Filonova for her expertise and technical assistance in analysing the dependency of *PWV* on vascular structural stiffness heterogeneity.

References

1. Mitchell GF, Parise H, Benjamin EJ, Larson MG, Keyes MJ, Vita JA, Vasan RS, Levy D. 2004 Changes in arterial stiffness and wave reflection with advancing age in healthy men and women: the Framingham Heart Study. *Hypertension.* **43**, 1239–1245. (doi:10.1161/01.HYP.0000128420.01881.aa)
2. Laurent S *et al.* 2006 Expert consensus document on arterial stiffness: methodological issues and clinical applications. *Eur. Heart J.* **27**, 2588–2605. (doi:10.1093/eurheartj/ehl254)
3. Lakatta EG, Wang M, Najjar SS. 2009 Arterial aging and subclinical arterial disease are fundamentally intertwined at macroscopic and molecular levels. *Med. Clin. North Am.* **93**, 583–604. (doi:10.1016/j.mcna.2009.02.008)
4. Ferruzzi J, Collins MJ, Yeh AT, Humphrey JD. 2011 Mechanical assessment of elastin integrity in fibrillin-1-deficient carotid arteries: implications for Marfan syndrome. *Cardiovasc. Res.* **92**, 287–295. (doi:10.1093/cvr/cvr195)
5. Ferruzzi J, Vorp DA, Humphrey JD. 2011 On constitutive descriptors of the biaxial mechanical behaviour of human abdominal aorta and aneurysms. *J. R Soc. Interface.* **8**, 435–450. (doi:10.1098/rsif.2010.0299)
6. Roccabianca S, Figueroa CA, Tellides G, Humphrey JD. 2014 Quantification of regional differences in aortic stiffness in the aging human. *J. Mech. Behav. Biomed. Mater.* **29**, 618–634. (doi:10.1016/j.jmbbm.2013.01.026)
7. Cuomo F, Roccabianca S, Dillon-Murphy D, Xiao N, Humphrey JD, Figueroa CA. 2017 Effects of age-associated regional changes in human central artery mechanics

on systemic hemodynamics revealed by computational modeling. *PLoS ONE* **12**, 1–21. (doi:10.1371/journal.pone.0173177)
8. Rammos C, Hendgen-Cotta UB, Deenen R, Pohl J, Stock P, Hinzmann C, Kelm M, Rassaf T. 2014 Age-related vascular gene expression profiling in mice. *Mech. Ageing Dev.* **135**, 15–23. (doi:10.1016/j.mad.2014.01.001)
9. Fleenor BS, Marshall KD, Durrant JR, Lesniewski LA, Seals DR. 2010 Arterial stiffening with ageing is associated with transforming growth factor-β1-related changes in adventitial collagen: reversal by aerobic exercise. *J. Physiol.* **588**, 3971–3982. (doi:10.1113/jphysiol.2010.194753)
10. Davis E. 1993 Stability of elastin in the developing mouse aorta: a quantitative radioautographic study. *Histochemistry* **100**, 17–26. (doi:10.1007/BF00268874)
11. Ferruzzi J, Bersi M, Mecham R, Ramirez F, Yanagisawa H, Tellides G, Humphrey JD. 2016 Loss of elastic fiber integrity compromises common carotid artery function: implications for vascular aging. *Artery Res.* **14**, 41–52. (doi:10.1016/j.artres.2016.04.001)
12. Wan W, Gleason RL. 2013 Dysfunction in elastic fiber formation in fibulin-5 null mice abrogates the evolution in mechanical response of carotid arteries during maturation. *Am. J. Physiol. Heart Circ. Physiol.* **304**, H674–H686. (doi:10.1152/ajpheart.00459.2012)
13. Ferruzzi J, Bersi MR, Uman S, Yanagisawa H, Humphrey JD. 2015 Decreased elastic energy storage, not increased material stiffness, characterizes central artery dysfunction in fibulin-5 deficiency independent of sex. *J. Biomech. Eng.* **137**, 031007. (doi:10.1115/1.4029431)
14. Gleason RL, Gray SP, Wilson E, Humphrey JD. 2004 A multiaxial computer-controlled organ culture and biomechanical device for mouse carotid arteries. *J. Biomech. Eng.* **126**, 787–795. (doi:10.1115/1.1824130)
15. CRIMSON. 2017 CardiovasculaR Integrated Modelling and SimulatiON. See http://www.crimson.software.
16. Sahni O, Müller J, Jansen KE, Shephard MS, Taylor CA. 2006 Efficient anisotropic adaptive discretization of the cardiovascular system. *Comput. Methods Appl. Mech. Eng.* **195**, 5634–5655. (doi:10.1016/j.cma.2005.10.018)
17. Figueroa CA, Vignon-Clementel IE, Jansen KE, Hughes TJR, Taylor CA. 2006 A coupled momentum method for modeling blood flow in three-dimensional deformable arteries. *Comput. Methods Appl. Mech. Eng.* **195**, 5685–5706. (doi:10.1016/j.cma.2005.11.011)
18. Cuomo F, Ferruzzi J, Humphrey JD, Figueroa CA. 2015 An experimental–computational study of catheter induced alterations in pulse wave velocity in anesthetized mice. *Ann. Biomed. Eng.* **43**, 1555–1570. (doi:10.1007/s10439-015-1272-0)
19. Baek S, Gleason RL, Rajagopal KR, Humphrey JD. 2007 Theory of small on large: potential utility in computations of fluid–solid interactions in arteries. *Comput. Methods Appl. Mech. Eng.* **196**, 3070–3078. (doi:10.1016/j.cma.2006.06.018)
20. Ferruzzi J, Bersi MR, Humphrey JD. 2013 Biomechanical phenotyping of central arteries in health and disease: advantages of and methods for murine models. *Ann. Biomed. Eng.* **41**, 1311–1330. (doi:10.1007/s10439-013-0799-1)
21. Les AS, Yeung JJ, Schultz GM, Herfkens RJ, Dalman RL, Taylor CA. 2010 Supraceliac and infrarenal aortic flow in patients with abdominal aortic aneurysms: mean flows, waveforms, and allometric scaling relationships. *Cardiovasc. Eng. Technol.* **1**, 39–51. (doi:10.1007/s13239-010-0004-8)
22. Stergiopulos N, Westerhof N. 1999 Role of total arterial compliance and peripheral resistance in the determination of systolic and diastolic aortic pressure. *Pathol. Biol. (Paris).* **47**, 641–647.
23. Simon AC, Safar ME, Levenson JA, London GM, Levy BI, Chau NP. 1979 An evaluation of large arteries compliance in man. *Am. J. Physiol.* **237**, H550–H554.
24. Xiao N, Alastruey J, Figueroa CA. 2014 A systematic comparison between 1-D and 3-D hemodynamics in compliant arterial models. *Int. J. Numer. Method Biomed. Eng.* **30**, 204–231. (doi:10.1002/cnm.2598)
25. Feintuch A *et al.* 2007 Hemodynamics in the mouse aortic arch as assessed by MRI, ultrasound, and numerical modeling. *Am. J. Physiol. Heart Circ. Physiol.* **292**, H884–H892. (doi:10.1152/ajpheart.00796.2006)
26. Greve JM, Les AS, Tang BT, Draney Blomme MT, Wilson NM, Dalman RL, Pelc NJ, Taylor CA. 2006 Allometric scaling of wall shear stress from mice to humans: quantification using cine phase-contrast MRI and computational fluid dynamics. *Am. J. Physiol. Heart Circ. Physiol.* **291**, H1700–H1708. (doi:10.1152/ajpheart.00274.2006)

27. Gaddum NR, Alastruey J, Beerbaum P, Chowienczyk P, Schaeffter T. 2013 A technical assessment of pulse wave velocity algorithms applied to non-invasive arterial waveforms. *Ann. Biomed. Eng.* **41**, 2617–2629. (doi:10.1007/s10439-013-0854-y)
28. Hartley CJ, Reddy AK, Madala S, Entman ML, Michael LH, Taffet GE. 2011 Doppler velocity measurements from large and small arteries of mice. *Am. J. Physiol. Hear. Circ. Physiol.* **301**, H269–H278. (doi:10.1152/ajpheart.00320.2011)
29. Womersley JR. 1955 XXIV. Oscillatory motion of a viscous liquid in a thin-walled elastic tube — I : The linear approximation for long waves. *Lond. Edin. Dublin Philos. Mag. J. Sci.* **46**, 199–221. (doi:10.1080/14786440208520564)
30. Womersley JR. 1955 Method for the calculation of velocity, rate of flow and viscous drag in arteries when the pressure gradient is known. *J. Physiol.* **127**, 553–563. (doi:10.1113/jphysiol.1955.sp005276)
31. Figueroa CA. 2006 A coupled-momentum method to model blood flow and vessel deformation in human arteries: applications in disease research and simulation-based medical planning. Chapter 2. Mathematics and physics of pulsatile flow in deformable vessels. PhD thesis, Stanford University, Stanford, CA, USA.
32. Nichols W, O'Rourke M, Vlachopoulos C. 1998 *McDonald's blood flow in arteries: theoretical, experimental and clinical principles*, 5th edn. New York, NY: Oxford University Press.
33. van de Vosse FN, Stergiopulos N. 2011 Pulse wave propagation in the arterial tree. *Annu. Rev. Fluid Mech.* **43**, 467–499. (doi:10.1146/annurev-fluid-122109-160730)
34. Laurent S, Boutouyrie P. 2015 The structural factor of hypertension: large and small artery alterations. *Circ. Res.* **116**, 1007–1021. (doi:10.1161/CIRCRESAHA.116.303596)
35. Humphrey JD, Harrison DG, Figueroa CA, Lacolley P, Laurent S. 2016 Central artery stiffness in hypertension and aging: a problem with cause and consequence. *Circ. Res.* **118**, 379–381. (doi:10.1161/CIRCRESAHA.115.307722)
36. Bellini C, Caulk AW, Li G, Tellides G, Humphrey JD. 2017 Biomechanical phenotyping of the murine aorta: what is the best control? *J. Biomech. Eng.* **139**, 044501. (doi:10.1115/1.4035551)
37. Le VP, Stoka KV, Yanagisawa H, Wagenseil JE. 2014 Fibulin-5 null mice with decreased arterial compliance maintain normal systolic left ventricular function, but not diastolic function during maturation. *Physiol. Rep.* **2**, 1–16.
38. Donato AJ, Walker AE, Magerko KA, Bramwell RC, Black AD, Henson GD, Lawson BR, Lesniewski LA, Seals DR. 2013 Life-long caloric restriction reduces oxidative stress and preserves nitric oxide bioavailability and function in arteries of old mice. *Aging Cell.* **12**, 772–783. (doi:10.1111/acel.12103)
39. Ferruzzi J, Madziva D, Caulk AW, Tellides G, Humphrey JD. 2018 Compromised mechanical homeostasis in arterial aging and associated cardiovascular consequences. *Biomech. Model. Mechanobiol.* **17**, 1281–1295. (doi:10.1007/s10237-018-1026-7)
40. Saouti N, Marcus JT, Vonk Noordegraaf A, Westerhof N. 2012 Aortic function quantified: the heart's essential cushion. *J. Appl. Physiol.* **113**, 1285–1291. (doi:10.1152/japplphysiol.00432.2012)
41. Humphrey JD, Eberth JF, Dye WW, Gleason RL. 2009 Fundamental role of axial stress in compensatory adaptations by arteries. *J. Biomech.* **42**, 1–8. (doi:10.1016/j.jbiomech.2008.11.011)
42. Hartley C *et al.* 2000 Hemodynamic changes in apolipoprotein E-knockout mice. *Am. J. Physiol. Heart Circ. Physiol.* **279**, H2326–H2334. (doi:10.1152/ajpheart.2000.279.5.H2326)
43. Huo Y, Guo X, Kassab GS. 2008 The flow field along the entire length of mouse aorta and primary branches. *Ann. Biomed. Eng.* **36**, 685–699. (doi:10.1007/s10439-008-9473-4)
44. Trachet B, Renard M, De Santis G, Staelens S, De Backer J, Antiga L, Loeys B, Segers P. 2011 An integrated framework to quantitatively link mouse-specific hemodynamics to aneurysm formation in angiotensin II-infused ApoE -/- mice. *Ann. Biomed. Eng.* **39**, 2430–2444. (doi:10.1007/s10439-011-0330-5)
45. Trachet B, Bols J, Degroote J, Verhegghe B, Stergiopulos N, Vierendeels J, Segers P. 2015 An animal-specific FSI model of the abdominal aorta in anesthetized mice. *Ann. Biomed. Eng.* **43**, 1298–1309. (doi:10.1007/s10439-015-1310-y)
46. De Wilde D, Trachet B, Debusschere N, Iannaccone F, Swillens A, Degroote J, Vierendeels J, De Meyer GRY, Segers P. 2016 Assessment of shear stress related parameters in the carotid bifurcation using mouse-specific FSI simulations. *J. Biomech.* **49**, 2135–2142. (doi:10.1016/j.jbiomech.2015.11.048)
47. Aslanidou L, Trachet B, Reymond P, Fraga-Silva RA, Segers P, Stergiopulos N. 2015 A 1D model of the arterial circulation in mice. *ALTEX* **33**, 13–28.

48. Segers P *et al.* 2005 Conductance catheter-based assessment of arterial input impedance, arterial function, and ventricular-vascular interaction in mice. *Am. J. Physiol. Heart Circ. Physiol.* **288**, H1157–H1164. (doi:10.1152/ajpheart.00414.2004)
49. Guo X, Kassab GS. 2003 Variation of mechanical properties along the length of the aorta in C57bl/6 mice. *Am. J. Physiol. Heart Circ. Physiol.* **285**, H2614–H2622. (doi:10.1152/ajpheart.00567.2003)
50. Robin F, Torsten L. 1931 The viscosity of blood in narrow capillary tubes. *Am. J. Physiol.* **96**, 562–568.
51. Cuomo F, Ferruzzi J, Agarwal P, Li C, Zhuang ZW, Humphrey JD, Figueroa CA. 2018 Data from: Sex-dependent differences in central artery hemodynamics in normal and fibulin-5 deficient mice: implications for aging. Dryad Digital Repository. (doi:10.5061/dryad.64c32m5)